

Research article

Photoacoustic tomography of intact human prostates and vascular texture analysis identify prostate cancer biopsy targets

Brittani L. Bungart^{a,b}, Lu Lan^c, Pu Wang^d, Rui Li^{a,d}, Michael O. Koch^e, Liang Cheng^f, Timothy A. Masterson^e, Murat Dundar^g, Ji-Xin Cheng^{c,h,*}

^a Weldon School of Biomedical Engineering, Purdue University, West Lafayette, IN, USA

^b Medical Scientist Training Program, Indiana University School of Medicine, Indianapolis, IN, USA

^c Department of Biomedical Engineering, Boston University, Boston, MA, USA

^d Vibronix Inc., West Lafayette, IN, USA

^e Department of Urology, Indiana University School of Medicine, Indianapolis, IN, USA

^f Department of Pathology and Laboratory Medicine, Indiana University School of Medicine, Indianapolis, IN, USA

^g Computer and Information Science Department, Indiana University-Purdue University Indianapolis, Indianapolis, IN, USA

^h Department of Electrical and Computer Engineering, Boston University, Boston, MA, USA

ARTICLE INFO

Keywords:

Photoacoustic imaging

Prostate

Targeted biopsy

K-means clustering

Texture image processing

ABSTRACT

Prostate cancer is poorly visualized on ultrasonography (US) so that current biopsy requires either a templated technique or guidance after fusion of US with magnetic resonance imaging. Here we determined the ability for photoacoustic tomography (PAT) and US followed by texture-based image processing to identify prostate biopsy targets. K-means clustering feature learning and testing was performed on separate datasets comprised of 1064 and 1197 nm PAT and US images of intact, *ex vivo* human prostates. 1197 nm PAT was found to not contribute to the feature learning, and thus, only 1064 nm PAT and US images were used for final feature testing. Biopsy targets, determined by the tumor-assigned pixels' center of mass, located 100% of the primary lesions and 67% of the secondary lesions. In conclusion, 1064 nm PAT and US texture-based feature analysis provided successful prostate biopsy targets.

1. Introduction

Prostate cancer (PCa) is the most incident, visceral cancer in USA men. An estimated 164,690 new prostate cancer cases are predicted to occur in 2018, which is 9.5% of all estimated 2018 cancer occurrences [1]. The current overall 5-year survival rate is 97.7%, especially when PCa is discovered at a local stage, but this drops to 30% if the PCa has metastasized prior to diagnosis [2]. In order to ensure that diagnosis occurs at the local stage while limiting harm to the patient, serum prostate-specific antigen (PSA) measurement is recommended as a screening tool for PCa depending on factors, such as age, family history and the patient's preference [3,4]. PSA is produced exclusively by prostate epithelial cells and can be influenced by benign conditions including: bacterial prostatitis [5], ejaculation [6], and benign prostatic hyperplasia [7]. Thus, false positive results from PCa serum PSA screening commonly occur, which makes a follow-up, confirmatory test necessary.

Currently to confirm the presence of PCa, histopathology analysis

with Gleason grading must be performed on biopsy samples acquired from the prostate in order to guide clinical decision making [8]. Gleason grading is based on the microscopic tissue architecture, and the two major Gleason grades are added to give the Gleason score [9]. The current clinical standard for acquiring biopsy samples is to perform a 12-core transrectal ultrasound (TRUS)-guided biopsy (TRUS-GB), which entails following a template to systematically acquire 12 tissue samples from the prostate [10]. To follow the template protocol, a TRUS probe guides the biopsy procedure by allowing visualization of the anatomical locations within the prostate [10,11]. Even with optimization of the TRUS-GB, false negative results occur in approximately 15–34% of initial biopsy procedures due to the limited, untargeted sampling of the prostate [12,13].

The combination of the PSA and the TRUS-GB is considered to be the major contributor to the overtreatment problem for PCa [3]. Since the biopsied tissue, and not the PSA, currently provides the diagnostic information to aid in therapeutic decision making [9], the biopsy procedure needs improvement due to its low sensitivity [14]. As previously

* Corresponding author at: Boston University Photonics Center, Boston University, 8 St. Mary's Street, Boston, MA, 02215, USA.

E-mail address: jxcheng@bu.edu (J.-X. Cheng).

<https://doi.org/10.1016/j.pacs.2018.07.006>

Received 6 February 2018; Received in revised form 24 June 2018; Accepted 26 July 2018

Available online 03 August 2018

2213-5979/ © 2018 The Authors. Published by Elsevier GmbH. This is an open access article under the CC BY-NC-ND license (<http://creativecommons.org/licenses/by-nc-nd/4.0/>).

mentioned, the current gold standard for performing the biopsy is a systematic approach based on a template [10]. Therefore, providing a target for the prostate biopsy may help to improve the sensitivity of the procedure.

The most notable clinical advancement for targeting the prostate biopsy is the magnetic resonance imaging-fusion biopsy (MRI-FB), which is currently recommended for patients undergoing repeat biopsy following an initial negative biopsy [15,16]. For biopsy-naïve patients, recent conflicting evidence exists regarding the PCa detection rate when using the MRI-FB compared to TRUS-GB [17–22]. Overall, these clinical studies show that the MRI-FB alone can reduce the number of cores needed to achieve the same PCa detection rates as the TRUS-GB [17,20,22]. Additionally, the MRI-FB has been shown to miss fewer clinically significant PCa tumors [22]. This reduction in cores needed and detection of clinically significant PCa tumors can reduce the risk of side effects and the need for repeat biopsy. However, many pitfalls exist with this method. Careful calibration is needed to fuse the real-time US and previously acquired, annotated multiparametric MRI (mpMRI). If the patient moves after alignment, the calibration must be completed again. In addition, the mpMRI images are static, and manual pressure on the prostate during biopsy can distort the tissue compared to the mpMRI [23]. Other pitfalls include added costs for the mpMRI [24] and the injected contrast agents, which may be contraindicated in some patients [25], used in the procedure. Thus, an ideal solution for targeting the PCa biopsy includes endogenous contrast and real-time, co-incident imaging and analysis.

Since the prostate biopsy is TRUS-guided, photoacoustic tomography (PAT), which uses traditional ultrasound (US) transducer arrays for signal collection [26], is a potential tool to apply clinically in order to improve the prostate biopsy. In contrast to MRI-FB, PAT has inherent co-registration with the US imaging channel as the PAT and US images are sequentially acquired using the same US transducer array. MRI-FB does have an advantage in imaging resolution and difference in biomarker type compared to PAT for prostate biopsy targeting. For PAT, the imaging resolution is dependent on the US transducer's imaging resolution [26]. Since the TRUS probe used for prostate biopsy is typically a low frequency US transducer with central frequency at approximately 7 MHz [27], the axial resolution is approximately two to three times lower than the resolution of the mpMRI sequences used for the MRI-FB [28]. Another potential major difference is that the recommended mpMRI utilizes two functional imaging sequences out of the three total sequences as biomarkers [28], while PAT approaches can be based on biomarker content [29,30] and/or functional alterations [31]. Overall, PAT should be investigated as an alternative to MRI-FB for the purpose of targeting the prostate biopsy.

The photoacoustic signal detected during PAT results when an absorber interacts with pulsed light in such a way that the energy is converted to heat, and the resultant local thermodynamic expansion releases an acoustic wave, which is detectable via an US transducer [26]. Compared to traditional optical-only imaging techniques, this allows for deeper imaging of major endogenous absorbers, such as deoxygenated and oxygenated hemoglobin, lipid, and water [26,30]. A few examples of the applications in which these endogenous photoacoustic contrast agents have been used are intravascular imaging of atherosclerotic plaques [32], breast cancer tumor margin assessment [33], and PCa [34] and breast cancer [35] vascularity. Since PCa is known to involve angiogenic processes [36], PAT, with hemoglobin as the endogenous contrast agent [26,30], may be able to identify targets for the prostate biopsy. Thus, we utilized the 1064 nm output from our previously published barium nitrite Raman laser [37] to image hemoglobin in human prostates. Unfortunately, angiogenesis in the prostate is not specific to PCa [36], while increasing cholesteryl ester, i.e. lipid, storage has been shown to be a specific biomarker to increasingly aggressive PCa [38]. Therefore, PAT was also performed at 1197 nm, which is an absorption peak for lipid [30,37].

Recent studies have begun applying PAT to the identification of PCa

in human prostates [34,39–41]. Unfortunately, a method of identifying targets for the prostate biopsy has yet to be achieved without manual selection of regions of interest (ROI) that rely on intensity-based thresholding [34,39] or the use of multispectral PAT analysis [39–41] that would decrease the frame rate. Out of these studies, Rajanna et al. used deep neural networks to learn features and then identify pixels representing PCa. This work was completed using a previously published PAT dataset of *ex vivo* human prostates that were sliced into axial sections prior to five wavelength PAT imaging [39]. The imaging method ensures uniform light fluence over the anterior-posterior axis of the tissue, which is currently not possible for prostate PAT in the clinical setting [34]. Additionally, the feature learning method used is based on feature learning of gene expression profiles, which can have hundreds of features [42]. Here, we minimize the PAT channels to 1064 and 1197 nm and acquire the standard US channel. Since feature learning typically involves 10 s–100 s of features [40,42], we utilize the “off-the-shelf” K-means clustering feature learning of texture patches, which has been shown to be effective in single-layer networks [43], for the purpose of identifying targets for PCa biopsy.

2. Materials and methods

2.1. Prostate specimen inclusion and handling

All work performed followed the approved Institution Review Board protocol (IUSCC-0581). A total of 9 prostate specimens were imaged in a room near the Indiana University Hospital surgical suite directly following radical prostatectomy (Fig. 1). After 10 sterile saline washes of the external surface, prostates were immobilized using an agar bed and imaged with PAT and US as described below. Formalin fixation and whole mount histopathological analysis was then performed by urogenital pathologist (L.C.) as previously described [44]. De-identified pathology reports were also provided in addition to the annotated whole mount histopathology slides.

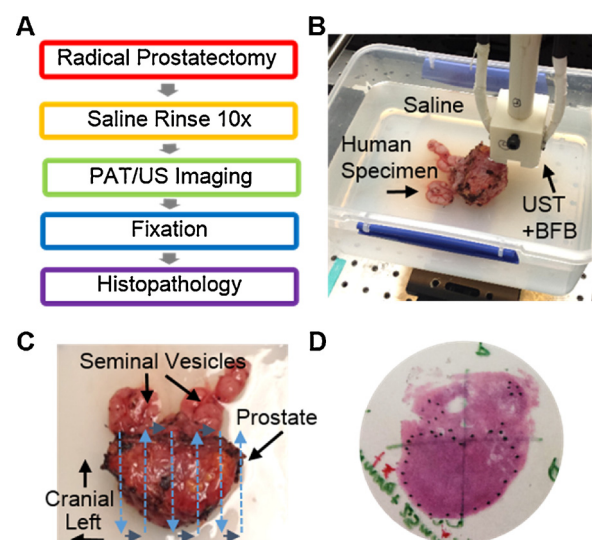


Fig. 1. Prostate Specimen Handling During Data Collection. (A) Prostate specimen handling procedure from radical prostatectomy to whole mount histopathology. (B) Image of prostate specimen during PAT and US imaging. UST + BFB: ultrasound transducer with bifurcated fiber bundle. (C) Image of prostate specimen depicting position during imaging and the raster scanning pathway. (D) Representative whole mount histopathology slide. An experienced urogenital pathologist marked the tumor margins and completed the corresponding histopathology report. These slides are considered ground truth for image analysis.

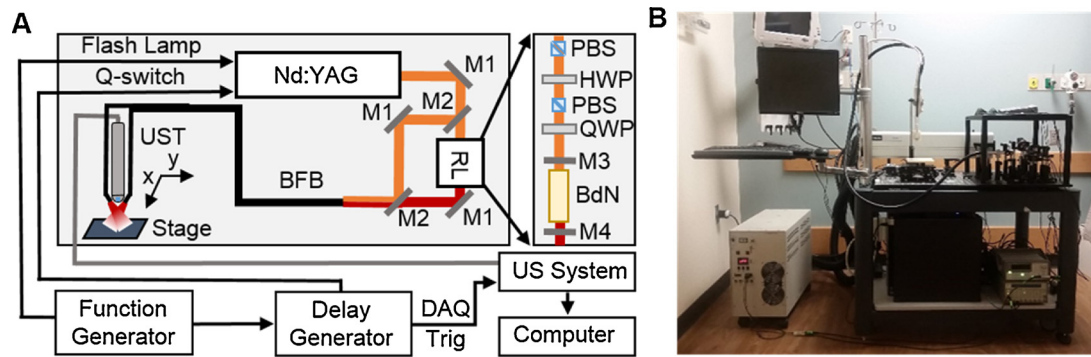


Fig. 2. Photoacoustic and Ultrasound Tomography Imaging Setup. (A) Schematic of PAT and US imaging system. M1: 45° reflective mirror; M2: flip-mounted 45° reflective mirror; M3: resonator end mirror; M4: output coupler; PBS: polarizing beam splitter; HWP: half wave plate; QWP: quarter wave plate; BdN: barium dinitrate crystal; BFB: bifurcated fiber bundle; UST: ultrasound transducer; DAQ: data acquisition system. (B) Image of PAT and US imaging system at location in Indiana University Hospital near surgical suite for optimized tissue handling.

2.2. PAT and US imaging

1064 nm and 1197 nm PAT imaging was performed using a setup (Fig. 2) with the previously published barium nitrite Raman laser [37] pumped with a 10 Hz Nd:YAG laser (Continuum, San Jose, CA). A bifurcated fiber bundle (Fiber Optic Systems, Inc., Simi Valley, CA) delivered the pulsed light at a 30° angle relative to the probe. A C9-5ICT TRUS probe (Philips, Andover, MA) was used to collect PAT signal and to perform US imaging with an US system (Verasonics, Kirkland, WA). The C9-5ICT TRUS probe was designed to include US imaging of the prostate from the rectal cavity, and thus allowed for imaging of the prostate's entire posterior-anterior depth. Experiments were performed at 55 mJ/pulse with a 0.5 mm step size while raster scanning. Scanning was performed in 10 min with no averaging applied per frame. Images were taken in the prostate's axial plane to match the histopathology slices' plane.

2.3. Image and histopathology slice matching

PAT and US images were matched to histopathology slides ($n = 40$) by using the US channel alone. Since the PAT and US imaging were performed in the same plane as the histopathology slides, the prostate characteristics from the histopathology slides, which included anterior-posterior length, left-right length, urethral position and perimeter shape, along with a minimum spacing of 4 mm between each prostate's histopathology slides, were used to determine the best match between the histopathology slides and the US channel. The measurements were taken manually from the histopathology slides [45]. Measurements of US channel frames were taken using ImageJ [46]. As scanning was performed in 0.5 mm increments, the distance between US channels was known to ensure at least 4 mm spacing between frames matched to consecutive histopathology slices.

2.4. Intensity-based analysis of PAT images

ImageJ was used to assess the minimum, average, and maximum signal intensities for PCa and laterally-matched benign ROIs. The averaged maximum benign ROI signal intensity was used as the minimum threshold for PCa-specific signal to determine if intensity thresholding can be applied to determine targets for the prostate biopsy.

2.5. Training and testing datasets

The training dataset consisted of six prostate specimens comprising of 28 total whole mount histopathology slices, while the testing dataset had three prostate specimens of 12 histopathology slices. Table 1 shows

Table 1

Patient characteristics of training and testing datasets.

Training Dataset (prostates = 6)	
Age	61 ± 9
Prostate Volume (cm ³)	82.3 ± 26.0
Primary Lesion Largest Dimension (cm)	2.79 ± 1.1
Secondary Lesion Largest Dimension (cm)	1.0 ± 0.4
Gleason 6	1
Gleason 7a	3
Gleason 7b	2
Gleason 8-10	0
Testing Dataset (prostates = 3)	
Age	72 ± 7
Prostate Volume (cm ³)	96.4 ± 23.3
Primary Lesion Largest Dimension (cm)	1.9 ± 1.0
Secondary Lesion Largest Dimension (cm)	1.2 ± 0.6
Gleason 6	0
Gleason 7a	2
Gleason 7b	1
Gleason 8-10	0

the specimens' clinical and pathological distribution. The two datasets were randomly divided, except for the Gleason 6 case that was specifically added to the training dataset as there was only one case with this Gleason score.

2.6. Statistical analysis

A minimum of three repetitions were used for all experiments. Values are represented as averages with standard deviation of sample for the error. One-way ANOVA was used for hypothesis testing with Tukey's HSD post hoc test. The significance level (p) is < 0.05.

3. Results

3.1. Performance of the PAT/US tomography system

In order to collect PAT and US images for testing our proposed image analysis approach, a PAT setup utilizing a TRUS probe was needed. Thus, we utilized the C9-5ICT TRUS probe, which is compatible with our US system. For PA excitation, we utilized a 10 Hz Nd:YAG laser to pump a barium nitrite Raman laser as we were testing 1064 and 1197 nm [37]. To deliver the pulsed light to the tissue, a bifurcated fiber bundle was fixed to the US probe at the end, parallel to the transducer array, with a 30° angle relative to the probe, thereby creating a focus of approximately 1 cm by 2 cm at 1 cm from the US transducer (Fig. 3A). The surface area per bifurcated fiber bundle end is

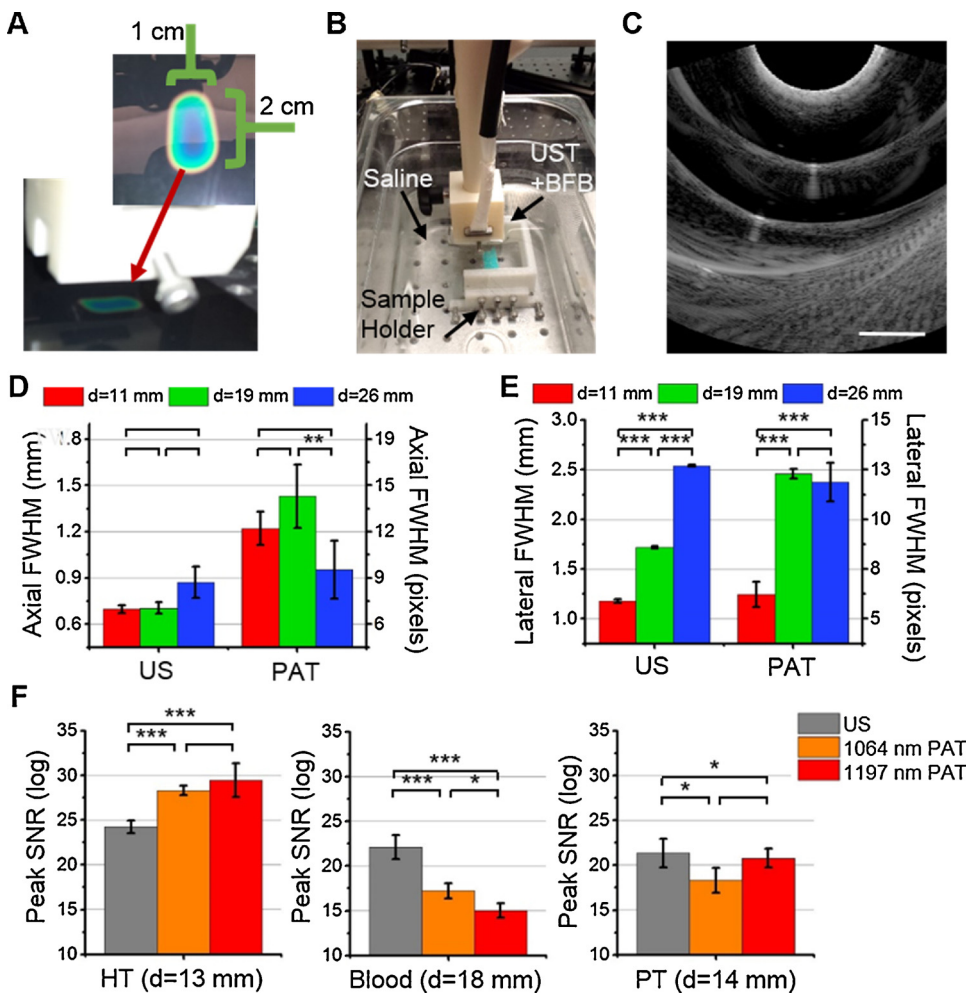


Fig. 3. Photoacoustic and Ultrasound Tomography Imaging System Performance. (A) Illumination area of 1064 and 1197 nm pulsed laser light at 1 cm from the fiber bundle ends. (B) Experimental setup to determine imaging resolution. UST + BFB: ultrasound transducer with bifurcated fiber bundle. (C) Representative US image of 25 μ m tungsten wire. Wires were centered relative to the transducer array for analysis. Each group has $n = 5$. Scale bar: 1 cm. (D,E) Axial and lateral resolution of the US and PAT system when imaging 25 μ m tungsten wire at depths (d) of 11, 19, and 26 mm below the US transducer array. (F) pSNR of 1064 and 1197 nm imaging of heat shrink tube (HT), polyethylene tube (PT), and coagulated human blood. Applies to all panels: each group has $n = 5$. * = $p < 0.05$; ** = $p < 0.001$; *** = $p < 0.0001$.

13 mm by 3 mm. With an energy output per bifurcated fiber bundle of 27.5 mJ/pulse, the total energy output was 55 mJ/pulse. Based on the fiber bundle end surface area and energy output, the energy density maximum was 70.5 mJ/cm². Thus, the fiber bundle setup and energy output is acceptable as the maximum permissible exposure for this laser is 100 mJ/cm² [47].

For PAT, the TRUS probe determines the imaging resolution. We assessed the C9-5ICT TRUS probe's US and PAT beam full width at half maximum (FWHM) with a custom sample holder (Fig. 3B) which contained 25 μ m tungsten wire at 11, 19, and 26 mm from the transducer (Fig. 3C). As expected, the US axial FWHM remained relatively constant over depth while the lateral FWHM increased (Fig. 3D and E). The PAT axial FWHM was larger compared to US while the PAT lateral FWHM was similar to US, except at 19 mm. These results are consistent with expected resolution for a TRUS transducer array with a center frequency of 7.8 MHz.

Lastly, the peak signal-to-noise ratio (pSNR) of the PA absorbers' US and 1064 nm and 1197 nm PAT were assessed using phantoms (Fig. 3F). Heat shrink tube (HT) is a broad-spectrum, strong absorber used here as a control, while polyethylene tube (PT) and coagulated human blood that was 1–2 h old in 1% agar gel was used for the prostate biomarkers of lipid and hemoglobin. The pSNR for blood was shown to be statistically different between all imaging channels. For HT and PT, pSNR for 1064 nm and 1197 nm PAT were not shown to be statistically different while a difference was shown between PAT and US channels.

3.2. Thresholding-based analysis is ineffective for identifying prostate cancer biopsy targets

Intensity thresholding for identifying PCa targets was initially applied due to recent *in vivo* PAT imaging study of prostate angiogenesis which utilized an intensity-based analysis [34]. For assessing intensity thresholding for identifying PCa-associated signal, we determined the minimum, average, and maximum signal intensities for PCa and depth-matched benign PAT ROIs (Fig. 4A). To include only PCa-specific signal after thresholding, the average maximum signal intensities for the 1064 nm and 1197 nm benign ROIs were used as the minimum cutoff for PCa-specific pixel identification. For 1064 nm PAT images, the threshold was set at 9.9 (log scale), while 8.8 was the threshold for 1197 nm PAT images. This approach results in no signal for identifying prostate biopsy targets in the PCa tissue (Fig. 4B and C). This is expected as the PCa and depth-matched benign ROIs' minimum, average, and maximum values are not statistically different (Fig. 4A). Based on these results, an alternative approach is needed for identifying targets for the prostate biopsy.

3.3. K-means clustering feature learning of PAT texture patches demonstrates that 1197 nm photoacoustic tomography does not uniquely contribute to clustering results

Besides intensity-based analysis, prior work involving PAT of human prostates for the purpose of distinguishing malignant versus benign tissue includes applying multispectral deconvolution, frequency analysis, and deep neural nets with Greedy feature selection to a dataset of axially-sectioned, *ex vivo* human prostates [39–41]. Unfortunately,

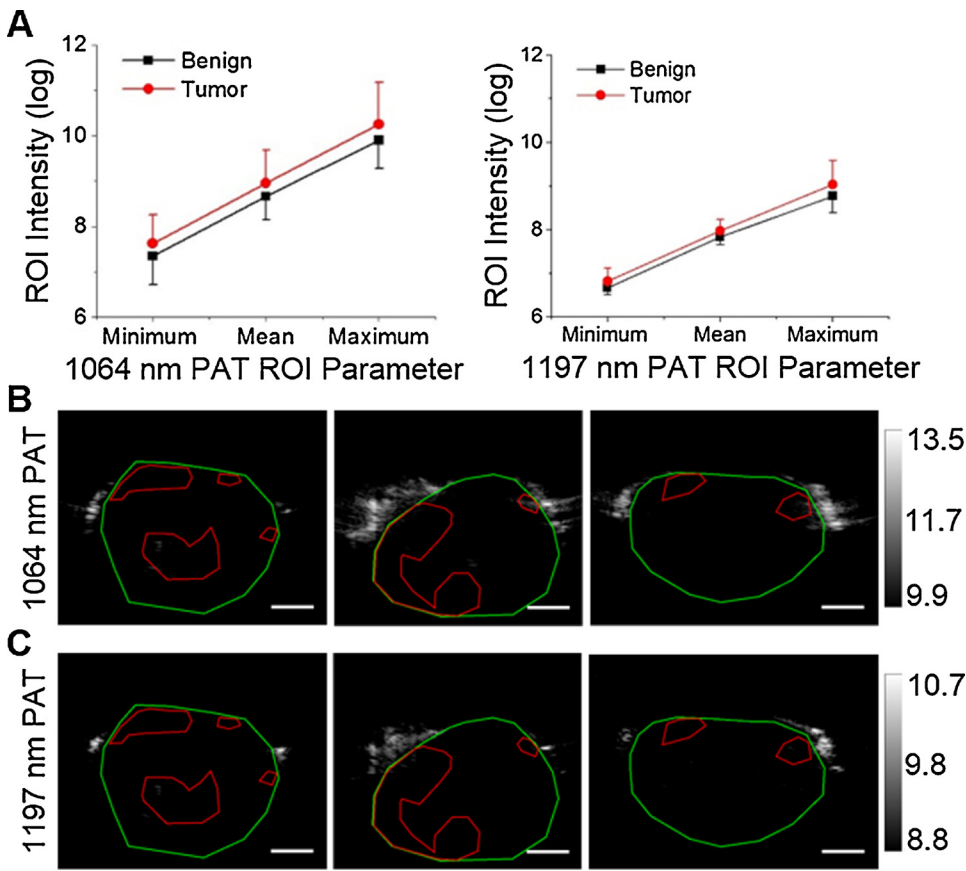


Fig. 4. Thresholding-based Analysis Is Ineffective for Identifying Prostate Cancer Biopsy Targets. (A) Signal intensity characteristics for tumor and matched benign ROI. Tumor and benign ROI were not statistically different. Each data point consists of at least $n = 12$. (B) 1064 nm and (C) 1197 nm representative PAT images that have been thresholded with the maximum average benign ROI measurement. Prostatic (green) and tumor tissue (red) are outlined. No biopsy targets were identified with this method of analysis. Applies to all panels: scale bar = 1 cm.

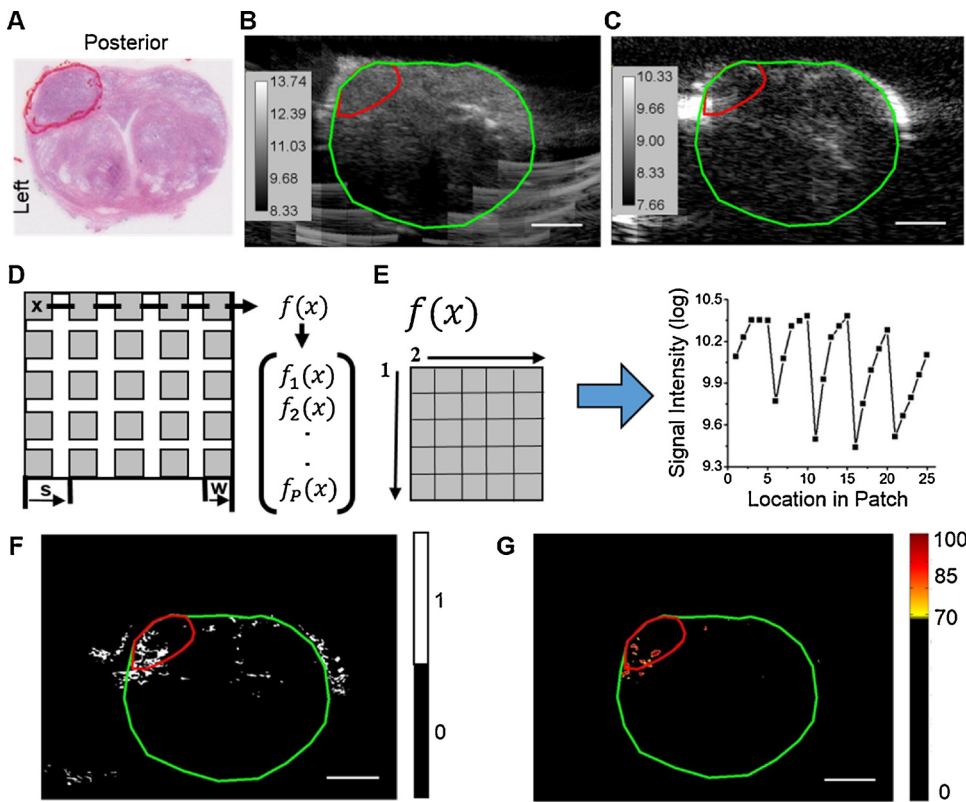


Fig. 5. Texture-based K-means Clustering Feature Learning. (A) Example whole mount histopathology slide with demarcated tumor margins (red line). (B) US and (C) 1064 nm PAT images that best match the whole mount histopathology slide in A are shown. (D) Texture patch (x) generation involves determining optimum patch size (w) and step size between patches (s). Patches are sequentially created from left to right and then top to bottom of the US and PAT images. (E) The patches are processed to a format that is appropriate for k-means clustering. (F) Raw PCA-related cluster output from k-means clustering feature learning of training set for US and PAT images in B and C. (G) Raw PCA-related cluster output converted to density heat map with thresholding. Signal corresponds to left posterior tumor foci in A. Applies to all panels: scale bar = 1 cm; Prostate margin: green line; Posterior tumor foci: red line.

multispectral deconvolution cannot be applied here as two PAT channels are not sufficient as there are at least three endogenous PA absorbers present, i.e. hemoglobin, lipid, and water [30]. Additionally,

with two PAT and one US imaging channel, we are limited in machine learning approaches without reformatting the data [42,43]. To reformat the data for k-means clustering feature learning, the

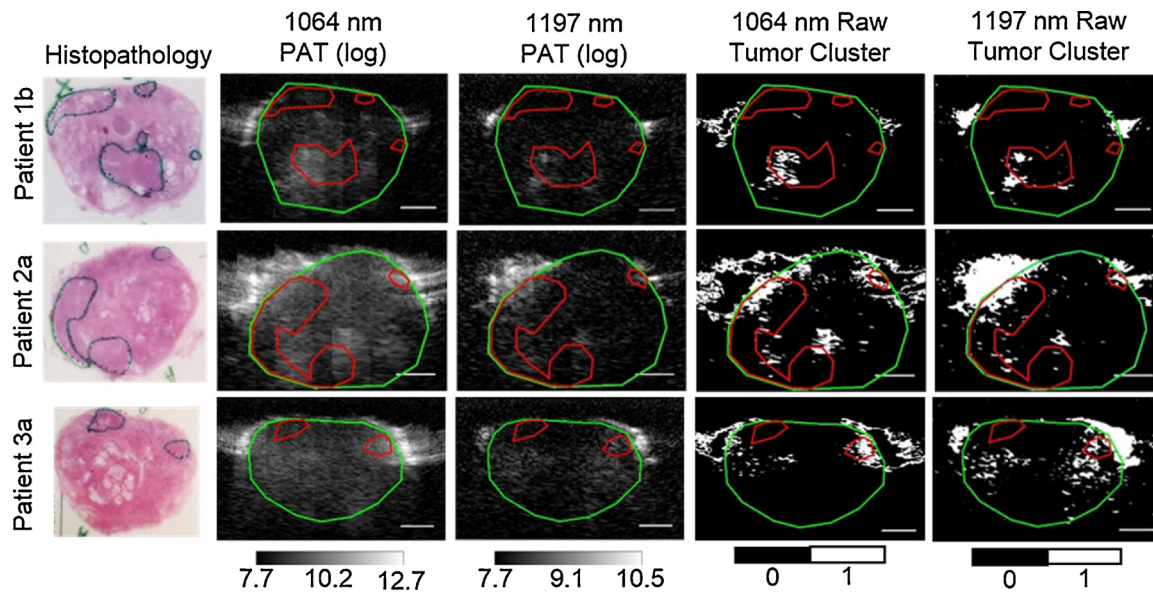


Fig. 6. 1197 nm Photoacoustic Tomography Does Not Uniquely Contribute to Clustering Results. Each PAT channel was tested for its contribution to PCa feature learning by viewing the results of the testing dataset. Whole mount histopathology slides with the major tumor's largest dimension from each case in the testing dataset are shown in the left-most column. The PCa tumor margins are outlined (green) on the histopathology slides by a urogenital pathologist. 1064 nm and 1197 nm PAT images in log scale corresponding to the histopathology slides are displayed in the second and third column with the prostate (green) and tumor margin (red) outlines matching the histopathology slides. The raw testing results are exhibited in the two right-most columns with the same prostate tissue (red) and tumor (red) outlines for reference. Applies to all panels: scale bar = 1 cm.

histopathology slice-matched PAT and US images (Fig. 5A–C) were initially converted from an image format to a format appropriate for k-means clustering (Fig. 5D and E). Texture patches were converted to row-wise data with neighborhood features in each column. The patches were five-by-five and considered column-wise from left to right. The step size between each patch was one. The patch size and step was chosen from prior published work [43]. Following reformatting the training dataset was dimensionally reduced using principal component analysis for the PAT channels alone. The top 50% of the major principal components were included for feature learning.

After reformatting and dimensionally reducing the data, the feature learning was performed using k-means clustering with the open source library VLFeat (0.9.20) [48] with $k = 100$. Since strong correlation between 1064 nm and 1197 nm PAT of hemoglobin and lipid was present (Fig. 3F), feature learning was performed on 1064 nm PAT with US and 1197 nm PAT with US (Fig. 6) to determine the clustering contribution from each PAT channel. The PCa-related features were manually chosen in the training dataset based on overlap with the PCa ROI in the ground truth histopathology slices. Next, the learned feature cluster centers were used to cluster the reformatted and dimensionally-reduced data in the testing dataset. The testing dataset was matched to the closest learned cluster center. The testing data that was clustered into the PCa-related feature clusters was then assessed for the clustering contribution.

As shown in Fig. 6, the original 1064 nm and 1197 nm PAT images are strongly correlated. For the testing cluster outputs, the PCa-related clusters are also similar except that there is more non-specific PCa cluster signal in the 1197 nm with US channel results, which could be due to the signal intensity being approximately an order of magnitude lower for the 1197 nm PAT versus the 1064 nm PAT (Fig. 6, Col. 2–3). Therefore, the 1197 nm PAT channel does not provide a unique contribution to identifying PCa biopsy targets, and only the 1064 nm PAT with US channel should be used for training and testing of prostate biopsy targets.

3.4. 1064 nm PAT and US texture analysis identifies biopsies targets

Since the learned features are not dependent upon the 1197 nm PAT channel, analysis was completed using the 1064 nm PAT and US channels. The cluster centers from the training dataset ($n = 28$) were used with the testing dataset ($n = 12$). As angiogenesis is not a specific biomarker [36], the PCa-associated clusters were not specific to PCa nor only prostatic tissue (Fig. 6). To overcome non-specific results, we apply a ten-by-ten density filter to the PCa cluster results. The ten-by-ten density filter is assignment of 0 to 100 to each pixel based on the number of pixels assigned to a PCa-related cluster in the nearby 10-by-10 pixels. Then, non-specific results were removed by thresholding the density level (Fig. 5G). Finally, the center of mass for groupings of prostatic signal was calculated to determine where the biopsy core would be targeted (Fig. 7).

Using center of mass on the density filter of the PCa cluster outputs, targets were successfully identified for 100% (3/3 prostates) of the primary PCa tumors in the testing dataset. In addition, 67% (2/3 prostates) of the secondary PCa tumors were targeted by this approach. A PCa-free histopathology slice was present in the testing dataset (Fig. 7). A small amount of PCa-associated cluster output was present in this PCa-free image. The signal was located in the bilateral peripheral posterior of the prostate. Since signal was present, biopsy targets were still included. Ultimately, the number of targets from our approach is ten, eight, and ten targets respectively for patient 1, 2, and 3 in the testing dataset. For these targets, the percentage of false positive cores was 40% (4/10), 50% (4/8), and 30% (3/10) cores for the three cases. Thus, we are able to target multiple locations of each PCa tumor in the cases with at least two fewer cores than the current clinical gold standard approach of the systematic 12-core TRUS-GB [11,49].

4. Discussion

Our work presented here shows that k-means clustering feature learning of 1064 nm PAT and US texture patches can be used to identify targets for prostate cancer biopsy. For the first time, PAT is utilized along with supervised machine learning to independently identify

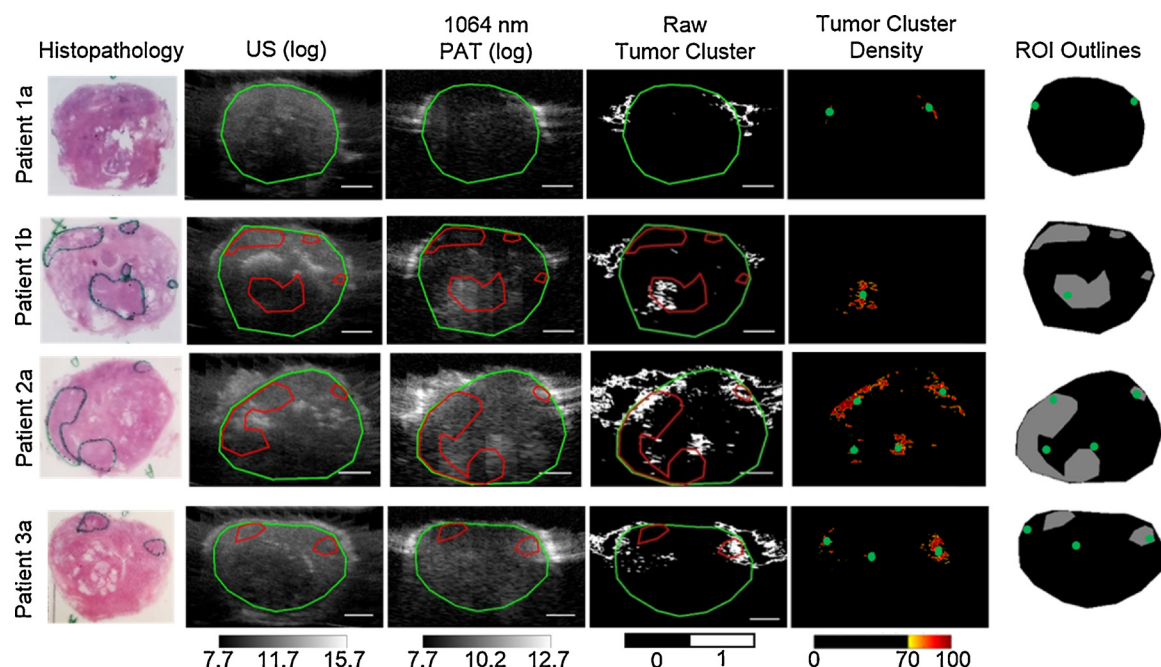


Fig. 7. Prostate Biopsy Targets Identified in Testing Dataset. The PCa tumor margins are outlined (green) on the whole mount histopathology slides in the left-most column. A cancer-free slide was present in patient 1 of the testing dataset. US and 1064 nm PAT images in log scale corresponding to the histopathology slides are displayed in the second and third column with the prostate (green) and tumor margin (red) outlines matching the histopathology slides. The raw testing results are exhibited in the fourth column with the same prostate tissue (red) and tumor (red) outlines for reference. The raw data is then shown as a density heat map in the fifth column. Center of mass (green circle) of the density signal marks the targets for hypothetical prostate biopsy core acquisition. In the right-most column, the location of these targets is displayed on the histopathology slides' ROI: prostatic tissue (black), prostate cancer (grey), and background (extraprostatic tissue and saline; white). Applies to all panels: scale bar = 1 cm.

targets for prostate biopsy in intact human specimens. Previously, significant work was performed on an axially-sliced human prostate specimen PAT dataset looking at multispectral deconvolution, frequency analysis, and deep neural nets with Greedy feature selection [39–41]. While this work shows the differences between PCa and benign prostate tissue, the studies' approaches are still based on user-selected ROIs or do not show the locations where targets would be suggested compared to ground truth histopathology slides. Additionally, the experimental design with sectioned prostate and subsequent transverse plane of imaging does not adequately challenge PAT and analysis methods on imaging depth that would be required for clinical translation. Most recently, an *in vivo* pilot study of three patients showed correlation of PAT of blood to vascular changes in prostate tissue with known PCa [34]. This work relied on intensity-only measurements which are limited over the depth of the prostate (Fig. 4). Thus, our work presented here provides an important contribution to the field of PAT of prostates for the purpose of guiding prostate cancer biopsy.

The analysis approach presented here has some inherent advantages as only a single PAT and the US channels were utilized. For PAT, pulsed lasers are necessary to stimulate the resulting acoustic signal [26]. These lasers are typically 10–20 Hz, with our system containing a 10 Hz laser. If multiple wavelengths or averaging was needed, the frame rate would then decrease and add more time to the procedure. The advantage of using multispectral PAT imaging is that deconvolution of the signal into its endogenous contrast components could be performed. Whereas, the benefit of averaging multiple frames at one imaging location is that the pSNR could be improved, which would improve the image quality for analysis. As the prostate biopsy is performed on awake patients and the urologist is manually controlling the US transducer while the patient can simultaneously move [50], issues with individual channels overlapping at an imaging location are possible. This alignment of individual channels is important for analysis purposes. Our image analysis approach avoids the potential issue of channel overlap in each frame as only a single PAT wavelength was ultimately

used to determine the prostate biopsy targets. The use of one PAT wavelength maximizes imaging speed and will limit added time for the procedure if clinically translated. Additionally, for the first time, we identify prostate biopsy targets with an imaging and light delivery scheme that is clinically relevant compared to previously published work [39–41].

For this preliminary study, inherent limitations are present. *Ex vivo* intact fresh prostate specimens were imaged directly after radical prostatectomy and before formalin fixation. The 1064 nm PAT images' signal is primarily from the endogenous absorber hemoglobin. The absorption coefficient of hemoglobin is different for oxy- versus deoxyhemoglobin [30]. As the prostate no longer has normal perfusion, we expect the feature learning of *in vivo* prostate 1064 nm PAT to provide different cluster centers than in the presented work. Additionally, an anatomical barrier that is not included in this study is the rectal wall, which is a highly scattering tissue [51]. Thus to ultimately prove the utility of this approach, *in vivo* imaging is necessary to see the analysis method's performance with normal anatomy and perfusion.

Another limitation in this study is the use of histopathology slices as ground truth for the biopsy targets. Differences in the thickness of the histopathology slides and the PAT/US image frames exist—histopathology slides are typically only a few microns thick, while the elevation resolution for TRUS transducers cannot achieve this thickness [52]. Also, our approach to matching was performed based on manual measurements [45]. Thus, exact matching for all of the histopathology slice to the appropriate PAT/US image frame is difficult to achieve.

A final consideration for this work is the light delivery and US transducer designs [26]. Here we utilize a bifurcated fiber bundle array at a 60° angle mounted to the US transducer. This design allows for the least amount of distance from the fiber bundle to the prostate tissue to limit light divergence and water absorption. However, a pitfall exists with this setup: an inherent focus of the light at approximately 1 cm from the fiber bundle and US transducer array (Fig. 3A). For this reason,

we believe that the secondary lesion that was not targeted in these results was due to the tumor's close proximity to the fiber bundle and US transducer. This issue could be overcome if an additional imaging scan was performed with the fiber bundle and TRUS probe farther from the tissue so that the most posterior tissue would be in the beams' focus. If this imaging modality and analysis were used clinically, the urologist could adjust the probe position in real-time to visualize the location.

5. Conclusions

1064 nm PAT and US texture-based k-means clustering feature learning successfully provided tumor cluster centers that were validated in the testing group. The resulting targets delivered a 100% (3/3) and 67% (2/3) sensitivity respectively to primary and secondary lesions while maintaining a total number of biopsy targets per prostate that is lower compared to the number of core biopsies acquired during current prostate biopsy protocols. Therefore, this real-time multimodal imaging technique with target identification method should be explored further *in vivo* to determine its clinical value for improving the sensitivity of prostate biopsies for the purpose of prostate cancer diagnosis.

Conflict of interest statement

The authors declare that there are no conflicts of interest. J.-X. C., P.W., and R.L. have a financial interest in Vibronix, Inc., which did not support this work.

Funding sources

This work was supported by the Walther Cancer Foundation and the National Institutes of Health (R41 CA192645, UL1TR001108).

References

- R.L. Siegel, K.D. Miller, A. Jemal, Cancer statistics, *CA Cancer J. Clin.* 68 (2018) 7–30, <https://doi.org/10.3322/caac.21442>.
- A. Noone, N. Howlander, M. Krapcho, D. Miller, A. Brest, M. Yu, J. Ruhl, Z. Tatalovich, A. Mariotto, D. Lewis, H. Chen, E. Feuer, K. Cronin, SEER Cancer Statistics Review, 1975–2015, Bethesda, MD, 2018, https://seer.cancer.gov/csr/1975_2015/.
- G.S. Sandhu, G.L. Andriole, Overdiagnosis of prostate cancer, *J. Natl. Cancer Inst. Monogr.* 2011 (2012) 146–151, <https://doi.org/10.1093/jncimonographs/lgs031>.
- J.J. Fenton, M.S. Weyrich, S. Durbin, Y. Liu, H. Bang, J. Melnikow, Prostate-Specific Antigen–Based Screening for Prostate Cancer: A Systematic Evidence Review for the U.S. Preventative Services Task Force. Evidence Synthesis No. 154. AHRQ Publication No. 17-05229-EF-1, Agency for Healthcare Research and Quality, Rockville, MD, 2018.
- D. Dalton, Elevated serum prostate-specific antigen due to acute bacterial prostatitis, *Urology* 33 (1989) 465.
- M.-B. Tchetchen, J.T. Song, M. Strawderman, S.J. Jacobsen, J.E. Oesterling, Ejaculation increases the serum prostate-specific antigen concentration, *Urology* 47 (1996) 511–516 <http://www.sciencedirect.com.proxy.medlib.uits.iu.edu/science/article/pii/S0090429599804865>.
- R.B. Nadler, P.A. Humphrey, D.S. Smith, W.J. Catalona, T.L. Ratliff, Effect of inflammation and benign prostatic hyperplasia on elevated serum prostate specific antigen levels, *J. Urol.* 154 (1995) 407–413, [https://doi.org/10.1016/S0022-5347\(01\)67064-2](https://doi.org/10.1016/S0022-5347(01)67064-2).
- Martin G. Sanda, Ronald C. Chen, Kirsten Greene, Laurence H. Klotz, Danil V. Makarov, M. Nelson, James Reston, George Rodrigues, Howard M. Sandler, M. Mary Ellen Taplin, Jeffrey A. Cadeddu, Clinically localized prostate cancer: American Urological Association (AUA)/American Society for Radiation Oncology (ASTRO)/Society of Urologic Oncology (SUO) Clinically localized prostate cancer, *Am. Urol. Assoc.* (2017) 1–56.
- J.I. Epstein, W.C.J. Allsbrook, M.B. Amin, L.L. Egevad, The 2014 International Society of Urological Pathology (ISUP) consensus conference on gleason grading of prostatic carcinoma, *Am. J. Surg. Pathol.* 40 (2016) 244–252, <https://doi.org/10.1097/01.pas.0000173646.99337.b1>.
- M.A. Bjurlin, H.B. Carter, P. Schellhammer, M.S. Cookson, L.G. Gomella, D. Troyer, T.M. Wheeler, S. Schlossberg, D.F. Penson, S.S. Taneja, Optimization of initial prostate biopsy in clinical practice: sampling, labeling and specimen processing, *J. Urol.* 189 (2013) 2039–2046, <https://doi.org/10.1016/j.juro.2013.02.072>.
- K. Hodge, Random systematic versus directed ultrasound guided transrectal core biopsies of the prostate, *J. Urol.* 142 (1989) 71–74 systematic versus directed ultrasound guided transrectal core biopsies <http://www.ncbi.nlm.nih.gov.proxy.medlib.uits.iu.edu/pubmed/holding=iussomlib&otool=iussomlib&term=random>.
- M.E. Chen, P. Troncoso, D.A. Johnston, K. Tang, R.J. Babaian, Optimization of prostate biopsy strategy using computer based analysis, *J. Urol.* 158 (1997) 2168–2175, [https://doi.org/10.1016/S0022-5347\(01\)68188-6](https://doi.org/10.1016/S0022-5347(01)68188-6).
- M.A. Levine, M. Itman, J. Melamed, H. Lepor, Two consecutive sets of transrectal ultrasound guided sextant biopsies of the prostate for the detection of prostate cancer, *J. Urol.* 159 (1998) 471–476, [https://doi.org/10.1016/S0022-5347\(01\)63951-X](https://doi.org/10.1016/S0022-5347(01)63951-X).
- H.G. Welch, E.S. Fisher, D.J. Gottlieb, M.J. Barry, Detection of prostate cancer via biopsy in the medicare-SEER population during the PSA era, *J. Natl. Cancer Inst.* 99 (2007) 1395–1400, <https://doi.org/10.1093/jnci/djm119>.
- A.B. Rosenkrantz, S. Verma, P. Choyke, S.C. Eberhardt, S.E. Eggner, K. Gaitonde, M.A. Haider, D.J. Margolis, L.S. Marks, P. Pinto, G.A. Sonn, S.S. Taneja, Prostate magnetic resonance imaging and magnetic resonance imaging targeted biopsy in patients with a prior negative biopsy: a consensus statement by AUA and SAR, *J. Urol.* 196 (2016) 1613–1618, <https://doi.org/10.1016/j.juro.2016.06.079>.
- P.R. Carroll, J.K. Parsons, G. Andriole, R.R. Bahnsen, E.P. Castle, W.J. Catalona, D.M. Dahl, J.W. Davis, J.I. Epstein, R.B. Etzioni, T. Farrington, G.P. Hemstreet, M.H. Kawachi, S. Kim, P.H. Lange, K.R. Loughlin, W. Lowrance, P. Maroni, J. Mohler, T.M. Morgan, K.A. Moses, R.B. Nadler, M. Poch, C. Scales, T.M. Shaneyfelt, M.C. Smaldone, G. Sonn, P. Sprenkle, A.J. Vickers, R. Wake, D.A. Shead, D.A. Freedman-Cass, Prostate cancer early detection, version 2.2016: featured updates to the NCCN guidelines, *JNCN J. Natl. Compr. Cancer Netw.* 14 (2016) 509–519, <https://doi.org/10.6004/jnccn.2016.0060>.
- M.M. Siddiqui, A.K. George, R. Rubin, S. Rais-Bahrami, H.L. Parnes, M.J. Merino, R.M. Simon, B. Turkbey, P.L. Choyke, B.J. Wood, P.A. Pinto, Efficiency of prostate cancer diagnosis by MR/ultrasound fusion-guided biopsy vs standard extended-sextant biopsy for MR-Visible lesions, *J. Natl. Cancer Inst.* 108 (2016) 1–7, <https://doi.org/10.1093/jnci/djw039>.
- A. Borkowetz, B. Hadaschik, I. Platzek, M. Toma, G. Torsev, T. Renner, R. Herout, M. Baumacke, M. Laniado, G. Baretton, J.P. Radtke, C. Kesch, M. Hohenfellner, M. Froehner, H.P. Schlemmer, M. Wirth, S. Zastrow, Prospective comparison of transperineal magnetic resonance imaging/ultrasonography fusion biopsy and transrectal systematic biopsy in biopsy-naïve patients, *BJU Int.* 121 (2018) 53–60, <https://doi.org/10.1111/bju.14017>.
- F. Porpiglia, M. Manfredi, F. Mele, M. Cossu, E. Bollito, A. Veltri, S. Cirillo, D. Regge, R. Faletti, R. Passera, C. Fiori, S. De Luca, Diagnostic pathway with multiparametric magnetic resonance imaging versus standard pathway: results from a randomized prospective study in biopsy-naïve patients with suspected prostate cancer, *Eur. Urol.* 72 (2017) 282–288, <https://doi.org/10.1016/j.eururo.2016.08.041>.
- V.K. Yarlagadda, W.S. Lai, J.B. Gordetsky, K.K. Porter, J.W. Nix, J.V. Thomas, S. Rais-Bahrami, MRI/US fusion-guided prostate biopsy allows for equivalent cancer detection with significantly fewer needle cores in biopsy-naïve men, *Diagn. Interv. Radiol.* 24 (2018) 115–120, <https://doi.org/10.5152/dir.2018.17422>.
- P.P. Tonttila, J. Lantto, E. Pääkkö, U. Piippo, S. Kauppila, E. Lammintausta, P. Ohtonen, M.H. Vaarala, Prebiopsy multiparametric magnetic resonance imaging for prostate cancer diagnosis in biopsy-naïve men with suspected prostate cancer based on elevated prostate-specific antigen values: results from a randomized prospective blinded controlled trial, *Eur. Urol.* 69 (2016) 419–425, <https://doi.org/10.1016/j.eururo.2015.05.024>.
- M.M. Siddiqui, S. Rais-Bahrami, H. Truong, L. Stamatakis, S. Vourganti, J. Nix, A.N. Hoang, A. Walton-Diaz, B. Shuch, M. Weintraub, J. Kruecker, H. Amalou, B. Turkbey, M.J. Merino, P.L. Choyke, B.J. Wood, P.A. Pinto, Magnetic resonance imaging/ultrasound-fusion biopsy significantly upgrades prostate cancer versus systematic 12-core transrectal ultrasound biopsy, *Eur. Urol.* 64 (2013) 713–719, <https://doi.org/10.1016/j.eururo.2013.05.059>.
- C.P. Filson, S. Natarajan, D.J.A. Margolis, J. Huang, P. Lieu, F.J. Dorey, R.E. Reiter, L.S. Marks, Prostate cancer detection with magnetic resonance-ultrasound fusion biopsy: the role of systematic and targeted biopsies, *Cancer* 122 (2016) 884–892, <https://doi.org/10.1002/cncr.29874>.
- M. Davuluri, A. Toler, A. Wojtowycz, G. Bratslavsky, S. Vourganti, Cost of prostate MRI-US fusion – a decision analysis comparing cost effectiveness of systematic transrectal ultrasound guided biopsy and mri-ultrasound fusion prostate biopsy in the initial and repeat biopsy setting, *J. Urol.* 193 (2015) e898–e899, <https://doi.org/10.1016/j.juro.2015.02.2550>.
- M. Perazella, Gadolinium-contrast toxicity in patients with kidney disease: nephrotoxicity and nephrogenic systemic fibrosis, *Curr. Drug Saf.* 3 (2008) 67–75, <https://doi.org/10.2174/157488608783333989>.
- L.V. Wang, J. Yao, A practical guide to photoacoustic tomography in the life sciences, *Nat. Methods* 13 (2016) 627–638, <https://doi.org/10.1038/nmeth.3925>.
- T.L. Szabo, P.A. Lewin, Ultrasound transducer selection in clinical imaging practice, *J. Ultrasound Med.* 32 (2013) 573–582, <https://doi.org/10.7863/jum.2013.32.4.573>.
- J.C. Weinreb, J.O. Barentsz, P.L. Choyke, F. Cornud, M.A. Haider, K.J. Macura, D. Margolis, M.D. Schnall, F. Shtern, C.M. Tempany, H.C. Thoeny, S. Verma, PI-RADS prostate imaging – reporting and data system: 2015, version 2, *Eur. Urol.* 69 (2016) 16–40, <https://doi.org/10.1016/j.eururo.2015.08.052>.
- J.R. Rajian, R. Li, P. Wang, J.-X. Cheng, Vibrational photoacoustic tomography: chemical imaging beyond the ballistic regime, *J. Phys. Chem. Lett.* 4 (2013) 3211–3215, <https://doi.org/10.1021/jz401638e>.
- J. Hui, R. Li, E.H. Phillips, C.J. Goergen, M. Sturek, J.X. Cheng, Bond-selective photoacoustic imaging by converting molecular vibration into acoustic waves, *Photoacoustics* 4 (2016) 11–21, <https://doi.org/10.1016/j.pacs.2016.01.002>.
- S. Hu, Emerging concepts in functional and molecular photoacoustic imaging, *Curr. Opin. Chem. Biol.* 33 (2016) 25–31, <https://doi.org/10.1016/j.cbpa.2016.04.003>.
- Y. Cao, A. Kole, J. Hui, Y. Zhang, J. Mai, M. Alloosh, M. Sturek, J.X. Cheng, Fast

- assessment of lipid content in arteries in vivo by intravascular photoacoustic tomography, *Sci. Rep.* 8 (2018) 1–10, <https://doi.org/10.1038/s41598-018-20881-5>.
- [33] R. Li, P. Wang, L. Lan, F.P. Lloyd, C.J. Goergen, S. Chen, J.-X. Cheng, Assessing breast tumor margin by multispectral photoacoustic tomography, *Biomed. Opt. Express* 6 (2015) 1273–1281, <https://doi.org/10.1364/BOE.6.001273>.
- [34] A. Horiguchi, M. Shinchi, A. Nakamura, T. Wada, K. Ito, T. Asano, H. Shinmoto, H. Tsuda, M. Ishihara, Pilot Study of Prostate Cancer Angiogenesis Imaging Using a Photoacoustic Imaging System, *Urology* 108 (2017) 212–219, <https://doi.org/10.1016/j.urolgy.2017.07.008>.
- [35] M. Heijblom, D. Piras, M. Brinkhuis, J.C.G. Van Hespren, F.M. Van Den Engh, M. Van Der Schaaf, J.M. Klaase, T.G. Van Leeuwen, W. Steenberg, S. Manohar, Photoacoustic image patterns of breast carcinoma and comparisons with Magnetic Resonance Imaging and vascular stained histopathology, *Sci. Rep.* 5 (2015) 1–16, <https://doi.org/10.1038/srep11778>.
- [36] G. Russo, M. Mischi, W. Scheepens, J.J. De La Rosette, H. Wijkstra, Angiogenesis in prostate cancer: onset, progression and imaging, *BJU Int.* 110 (2012) 794–808, <https://doi.org/10.1111/j.1464-410X.2012.11444.x>.
- [37] R. Li, M.N. Slipchenko, P. Wang, J.-X. Cheng, Compact high power barium nitrite crystal-based Raman laser at 1197 nm for photoacoustic imaging of fat, *J. Biomed. Opt.* 18 (2013) 040502, <https://doi.org/10.1117/1.JBO.18.4.040502>.
- [38] S. Yue, J. Li, S.-Y. Lee, H.J. Lee, T. Shao, B. Song, L. Cheng, T.A. Masterson, X. Liu, T.L. Ratliff, J.-X. Cheng, Cholesteryl ester accumulation induced by PTEN loss and PI3K/AKT activation underlies human prostate cancer aggressiveness, *Cell Metab.* 19 (2014) 393–406, <https://doi.org/10.1016/j.cmet.2014.01.019>.
- [39] V.S. Dogra, B.K. Chinni, K.S. Valluru, J.V. Joseph, A. Ghazi, J.L. Yao, K. Evans, E.M. Messing, N.A. Rao, Multispectral photoacoustic imaging of prostate cancer: preliminary ex-vivo results, *J. Clin. Imaging Sci.* 3 (2013) 41, <https://doi.org/10.4103/2156-7514.119139>.
- [40] A.R. Rajanna, R. Ptucha, S. Sinha, B. Chinni, V. Dogra, N.A. Rao, Prostate cancer detection using photoacoustic imaging and deep learning, *IS&T Int. Symp. Electron. Imaging* (2016) 1–6, <https://doi.org/10.2352/ISSN.2470-1173.2016.15.IPAS-189>.
- [41] S. Sinha, N.A. Rao, B.K. Chinni, V.S. Dogra, Evaluation of frequency domain analysis of a multiwavelength photoacoustic signal for differentiating malignant from benign and normal prostates: ex vivo study with human prostates, *J. Ultrasound Med.* 35 (2016) 1–13, <https://doi.org/10.7863/ultra.15.09059>.
- [42] R. Fakoor, F. Ladhak, A. Nazi, M. Huber, Using deep learning to enhance cancer diagnosis and classification, *Proceeding 30th Int. Conf. Mach. Learn.* (2013) 28.
- [43] A. Coates, A. Arbor, A.Y. Ng, An analysis of single-layer networks in unsupervised feature learning, *Aistats* (2011) 215–223, <https://doi.org/10.1109/ICDAR.2011.95>.
- [44] R. Arora, M.O. Koch, J.N. Eble, T.M. Ulbright, L. Li, L. Cheng, Heterogeneity of Gleason grade in multifocal adenocarcinoma of the prostate, *Cancer* 100 (2004) 2362–2366, <https://doi.org/10.1002/cncr.20243>.
- [45] M. Heijblom, D. Piras, M. Brinkhuis, J.C.G. van Hespren, F.M. van den Engh, M. van der Schaaf, J.M. Klaase, T.G. van Leeuwen, W. Steenberg, S. Manohar, Photoacoustic image patterns of breast carcinoma and comparisons with Magnetic Resonance Imaging and vascular stained histopathology, *Sci. Rep.* 5 (2015) 11778, <https://doi.org/10.1038/srep11778>.
- [46] C.A. Schneider, W.S. Rasband, K.W. Eliceiri, NIH Image to ImageJ: 25 years of image analysis, *Nat. Methods* 9 (2012) 671–675, <https://doi.org/10.1038/nmeth.2089>.
- [47] ANSI Z136.1, *Safe Use of Lasers*, American National Standards Institute, Inc., 2007.
- [48] A. Vedaldi, B. Fulkerson, *VLFeat: An Open and Portable Library of Computer Vision Algorithms*, (2008).
- [49] O. Ukimura, J.A. Coleman, A. De La Taille, M. Emberton, J.I. Epstein, S.J. Freedland, G. Giannarini, A.S. Kibel, R. Montironi, G. Ploussard, M.J. Roobol, V. Scattoni, J.S. Jones, Contemporary role of systematic prostate biopsies: indications, techniques, and implications for patient care, *Eur. Urol.* 63 (2013) 214–230, <https://doi.org/10.1016/j.eururo.2012.09.033>.
- [50] A. El-Hakim, S. Moussa, CUA guidelines on prostate biopsy methodology, *Can. Urol. Assoc. J.* 4 (2010) 89–94.
- [51] S. Tang, J. Chen, P. Samant, S. Kelly, L. Xiang, Transurethral photoacoustic endoscopy for prostate cancer: a simulation study, *IEEE Trans. Med. Imaging* 35 (2016) 1780–1787, <https://doi.org/10.1109/TMI.2016.2528123>.
- [52] D. Lieu, Ultrasound physics and instrumentation for pathologists, *Arch. Pathol. Lab. Med.* 134 (2010) 1541–1556, <https://doi.org/10.1043/2009-0730-RA.1>.



Brittani L. Bungart is currently a M.D./Ph.D. student at the Indiana University School of Medicine and Purdue University's Weldon School of Biomedical Engineering's Medical Scientist Training Program. She received her B.S. in Biological Engineering from the University of Missouri in 2012. She joined the Ji-Xin Cheng Lab at Purdue University as a Ph.D. student in 2015, where her research is focused on the application of photoacoustic tomography to prostate cancer diagnosis.



Lu Lan is currently a Ph.D. student of Biomedical Engineering at Boston University. He received his B.Sc. from South China University of Technology (Guangzhou, China) in 2011, and MEng degree in Optical Engineering at Zhejiang University (Hangzhou, China) in 2014. He joined Cheng Lab as a Ph.D. student in 2014, where his research is focused on vibrational photoacoustic imaging and tomography, and translation of bio-photonics devices into clinics.



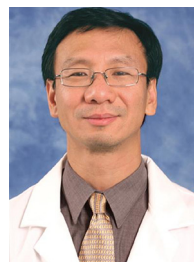
Pu Wang is currently working in Vibronix Inc. He received his Ph.D. in 2014 from Weldon School of Biomedical engineering at Purdue University with expertise in multimodal microscopy and photoacoustic imaging. In his current position, he developed multiple imaging and sensor technologies for disease diagnosis and treatment.



Rui Li is currently working in Vibronix Inc. He received his PhD in 2017 from Weldon School of Biomedical Engineering at Purdue University with expertise in laser technology and photoacoustic imaging. In his current position, he develops multimodal photoacoustic/ultrasound tomography for disease diagnosis.



Michael O. Koch has been chair of the Department of Urology at Indiana University School of Medicine since 1998. He completed his M.D. at Dartmouth Medical School in 1981 and residency training in urology at Vanderbilt University Medical Center in 1987. His clinical and academic interests include bladder and prostate cancer. He has studied multiple techniques to improve the outcomes in surgical management of prostate cancer, including both early and late state disease, and is known for his role in pioneering high intensity focused ultrasound for prostate cancer treatment.



Liang Cheng is the Virgil Moon Professor of Pathology at the Indiana University School of Medicine. He completed his M.D. at the Beijing Medical University in China followed by residency training in pathology at the Case Western Reserve University and a fellowship in urologic surgical pathology at Mayo Clinic. His research interests include molecular diagnostics and molecular genetic pathology in urology.



Timothy A. Masterson is an associate professor in the Department of Urology at the Indiana University School of Medicine (IUSM). He completed his M.D. at IUSM in 2001. After residency training in urology at the University of Utah in Salt Lake City, he completed a fellowship in urological oncology at Memorial-Sloan Kettering Cancer Center in New York City. His clinical specialization includes treatment of adult genitourinary cancers and reconstruction.



Ji-Xin Cheng is currently the Moustakas Chair Professor in Photonics and Optoelectronics, professor of Biomedical Engineering, and professor of Electrical and Computer Engineering at Boston University, Boston, Massachusetts. He received his B.S and Ph.D. degrees from the Department of Chemical Physics, University of Science and Technology of China, Hefei, China, in 1994 and 1998, respectively. His research lab at Boston University is devoted to the research of development of label-free molecular spectroscopic imaging tools, discovery of new biology at single cell level, and development of medical devices for early molecule-based diagnosis and surgery guidance.



Murat Dundar is an Associate Professor at the Department of Computer and Information Science, Indiana University–Purdue University Indianapolis, IN, USA. His research expertise is in machine learning with a focus on nonparametric Bayesian models and inference. His research interests mainly include real-world problems in computer-aided diagnosis/detection, hyper-spectral data analysis and remote sensing, biodetection, flow cytometry data analysis, information retrieval, and topic modeling.